Characterization of blood velocity in arteries using a combined analytical and Doppler imaging approach

Bchara Sidnawi, Zhen Chen, Chandra Sehgal, Sridhar Santhanam, and Qianhong Wu

Phys. Rev. Fluids **4**, 053101 — Published 13 May 2019

DOI: 10.1103/PhysRevFluids.4.053101

Characterization of blood velocity in arteries using a combined analytical and doppler imaging approach

Bchara Sidnawi, M.S[a,b], Zhen Chen, M.D[c], Chandra Sehgal, Ph.D[c], Sridhar Santhanam, Ph.D[a], Qianhong Wu, Ph.D[a,b*]

[a] *Department of Mechanical Engineering, Villanova University, PA19085, USA*

[b] *Cellular Biomechanics and Sport Science Laboratory, Villanova University, PA19085, USA*

[c] *Department of Radiology, University of Pennsylvania, PA19104, USA*

[*] Corresponding author: Qianhong Wu, PhD. Email: qianhong.wu@villanova.edu

Tel: +1-610-519-8969

Address for correspondence:

800 Lancaster Ave.

Department of Mechanical Engineering

Villanova University

PA 19085, USA

Receipt date:

10/04/2018

Abstract

We report a novel experimental and analytical approach to characterize the pulsatile blood flow field based on Doppler ultrasound imaging of the carotid and brachial arteries. The diameter-averaged (DA) velocity, obtained from the instantaneous velocity histograms extracted from the Doppler waveform, was adapted to the solution of a pulsatile flow in a pipe; from which the instantaneous velocity profiles were predicted and compared to local velocity measurements in the carotid and brachial arteries of four healthy human subjects. Very good agreement as demonstrated by the regression slope of 0.97 and near-zero intercept was observed between the spatiotemporal flow field predictions and local velocity measurements at specific distances from the vessel wall. Near-real-time *in vivo* measurements statistically demonstrate that, the novel analytical and experimental approach presented herein precisely captures the pulsatile blood flow behavior in large blood vessels.

Key Words: Wall Shear Stress, Ultrasound Imaging, Pulsatile flow

1. Introduction

Extensive studies have shown that the wall shear stress (WSS) is a major mechanical modulator of many functions in the cardiovascular system. With the assistance of duplex Doppler ultrasound imaging, we aim to develop a comprehensive experimental and analytical approach based on a pipe pulsatile flow to determine the instantaneous velocity field at specific streamwise locations in arteries, as it is the only factor, aside from blood viscosity, that determines WSS.

1.1. Significance of WSS

Endothelial function relies on the mechanical signals from WSS maintaining cell homeostasis and in adapting to the environmental changes around the endothelial cells of blood vessels. The adaptive response of endothelial cells to the changing shear and stretch load imposed by the flow in blood vessels was examined and it was observed that living cells react to changes in their micro-environments to maintain their “well-being”, also referred to as “the wisdom of the cell” [1]. The mechanism underlying mechano-transduction by the endothelial glycocalyx layer, a negatively charged layer of proteoglycan, glycoprotein and glycosaminoglycans, was investigated where it was shown that the flexural rigidity of the core proteins is small enough to be compressed easily and yet big enough to make those proteins adequate transducers of the WSS [2,3]. Smooth muscle cell marker genes have been found to be modulated by the WSS following a vascular injury [4]. Complex spatiotemporal WSS in regions where the flow is disturbed near arterial bifurcations lead to atherosclerosis susceptibility [5]. Several vascular pathology studies [6-9] have shown low average WSS to be a plaque-modulating factor.

The laboratory observations have been supported by several clinical studies that emphasize the importance of monitoring WSS in predicting, characterizing, and treating numerous cardiovascular diseases including aortic dilation or valvular stenosis [10], dilation and dissection in arteries [11,12], aortic stenosis [13], asymptomatic carotid plaque [14], coronary atherosclerosis [15], arteriovenous malformation (AVM) [16]. Additionally, cognitive impairment in old patients has been found to be correlated with WSS in the common carotid artery [17]. Altered WSS caused by prolonged sitting has been shown to be underlying endothelial dysfunction and impairment of the flow-mediated dilation of the popliteal artery in legs [18]. A differential regulation of flow and WSS was observed in the carotid and brachial arteries, in response to water immersion of the human body [19]. A new family of cardiovascular risk indicators for the assessment of WSS spatiotemporal patterns, was introduced [20] and proved to be more appropriate than the oscillatory shear index (OSI).

1.2. WSS Assessment

In the context of the discussion above, accurate and quantitative assessment of WSS is of high priority. WSS can be either evaluated based on time-resolved 3D phase contrast Magnetic Resonance Imaging (better known as 4D-MRI) or calculated through image-based Computational Fluid Dynamics (CFD) simulation. In 4-Dimensional Magnetic Resonance Imaging (4D-MRI) [10,12,14,16], the artery is first segmented, local velocity components are measured within the set spatial and temporal resolutions, from which local WSS distributions are estimated. However, the MRI approach may underestimate the magnitude of WSS due to the limited spatial resolution [14, 21]. One may argue that increased spatial resolution of MRI can potentially improve the accuracy

of WSS measurement, while this would make the approach even more expensive and requires long imaging time.

As an alternative approach, the CFD methods [14,15] use computerized axial tomography (CAT scans) or Magnetic Resonance Angiography (MRA) to construct the artery geometry specific to each patient and compute the flow field by solving the Navier-Stokes equations. However, it also has several limitations in the assessment of pulsatile flow and WSS. The first crucial aspect concerns the quality of reconstructing the geometry based on the image data (CT or MRI). Many studies applied smoothing filters to the reconstructed geometries to ensure the quality of volume mesh and computational efficiency [22] which inevitably introduces mismatches between the reconstructed geometry and the true geometry. The second issue is the setup of boundary conditions in the numerical simulation. It is not realistic to simulate the whole cardiovascular system, and thus the regional simulation of blood flow requires appropriate physiological conditions at inlet and outlets [23] Because of this, the physiological parameters applied to the boundaries (pressure difference, volume flow rate, etc.) might be different from the real flow conditions. Besides, the image-based CFD is a time-consuming approach, it may take hours of labor to convert medical images to 3D geometries [24] and require a huge amount of computer time to conduct the simulation.

These aforementioned limitations will be mitigated in the current study.

1.3. Doppler Ultrasound Imaging with Applications to WSS Estimation

With typical spatial and temporal resolutions ranging from 0.5 to 1 mm and 5 to 10 ms, respectively, Doppler ultrasound allows monitoring of systolic velocities to detect vascular diseases such as large-artery occlusive disease and fetal compromise [25,26]. Vector ultrasound technique has been used for a better visualization of the blood flow complexity that directly affects WSS [27]. But it is more expensive than the traditional spectral Doppler imaging (still substantially cheaper than MRI). On the other hand, in Ref. [28] C-plane Doppler was used to estimate the blood flow in the lower abdominal vessels of a porcine model. The measurements were performed using a matrix array transducer system. The results were compared to readings from a surgically implanted ultrasonic transit-time flow probe. Good agreement was found between the two techniques. Because the C-plane Doppler is both non-invasive and relatively cheaper, it is adopted in the current study.

As a reliable blood flow data acquisition technique, Doppler ultrasound has been coupled with Womersley's analytical solution [29] to a pulsatile flow in a rigid pipe, as well as CFD methods to estimate the velocity profile, WSS, and blood flow rate. For example, Maximum Doppler velocity, based on the maximum spectral velocity detected, has been combined with the Womersley's equations to predict the velocity profile [30-31]. Some correction factor was suggested [26] to this method for a better flow rate estimation. However, the correction did not cover WSS estimation. On the other hand, computer simulated ultrasound experiments were performed using computational blood flow data to assess the accuracy of Doppler imaging [33]. The computation was done by introducing particles in the flow field to mimic red blood cells, and then computationally generating the Doppler signal that would result from bouncing ultrasound waves off

these particles. It was found that mean velocity tracking is more successful than peak velocity tracking. Nevertheless, this method relies heavily on the computational methods. The same limitation is found in other studies [34-36]. Alternatively, vascular phantoms, an apparatus consisting of components that mimic blood vessels embedded under human tissue, have been employed where the Doppler detected centerline velocity was used in Womersley's model to obtain the flow rate and shear stress [35-37]. The problem with this method is that it infers the velocity profile based on velocity readings from a very narrow central region in the blood vessel, making the prediction more likely to be thrown off by any fluctuation in the profile shape towards asymmetry.

The main limitations to all the above-mentioned studies about Doppler ultrasound WSS estimation, are that they either rely on synthetic Doppler data based on CFD methods, or vascular phantoms. That is on top of the reliance on the centerline velocity as an input to Womersley's model, making both the flow rate and WSS prone to overestimation [36].

1.4. Focus of the current study

In the present work, these limitations are treated by in vivo, near-real-time validation of the estimated velocity profile that was based on a more appropriate and carefully interpreted input from Doppler data to Womersley's equations. The study integrates the spectral Doppler velocity measurements with the classical Womersley's model to estimate the velocity field and the WSS in arteries with two major differences. First, the calculations are based on the measured instantaneous mean velocity averaged across the entire diameter of the artery (DA). That is, instantaneous velocity histograms derived from Doppler waveforms are used rather than just the peak Doppler

velocity (VC). The advantage of the DA velocity is that it takes into consideration the entire flow behavior over the cross-section. Under a reasonable assumption that red blood cells are uniformly distributed over the diameter of the vessel, the mean velocity trace of spectral Doppler is translated mathematically into an expression that can be incorporated in Womersley's model. Also, as explained later, the time-averaged mean velocity (TAMn) trace was not interpreted to be the flow-averaged velocity that would yield the flow rate when multiplied by the cross-sectional area. Instead, it was treated as the arithmetic mean of the velocity along the diameter, which is not the same as the flow-averaged velocity for a circular cross-section. The second difference is that local velocity measurements were performed to validate the predicted velocity profiles, rather than using a CFD model. As will be shown later in this paper, this novel experimental and analytical approach is statistically proven to be more reliable than using just the centerline velocity. In most of the cases, both temporal and spatial predictions of the velocity profiles agree very well with local measurements.

2. Experiments

2.1. Whole-vessel spectral Doppler

The study was performed on 4 healthy subjects whose ages ranged from 27 to 68 years old. Vascular ultrasound imaging of the brachial and carotid arteries was performed with the subjects lying supine, exposing the arm or neck. Images were acquired with a Zonare ZS3 scanner (ZONARE Medical Systems, Bernardo, CA, USA) using a broadband high resolution L14-5 MHz hockey stick transducer or L14-5 MHz wide linear array transducers. The experimental protocol was approved by the institutional review committee and informed consent for the study was obtained from all

185 human subjects in accordance with the WORLD Medical Association Declaration of
186 Helsinki: Ethical principles for medical research involving human subjects, 2008.

187 The artery was first located using a cross-sectional view (Fig. 1a) and then,
188 switched to a chosen longitudinal plane of the artery. The diameter was measured from
189 the ultrasound image before the Doppler mode was turned on. Since the Doppler effect
190 is due to the head-on component of the velocity relative to the ultrasound beam which
191 would be zero if the angle was 90 degrees, the sample line of Doppler measurement
192 (the short line in Fig 1b) was set in an orientation that was as close to being parallel to
193 the flow direction as possible, while the Doppler insonation angle (the angle between
194 the ultrasound beam and the sample line in Fig 1b) was set to be under 60 degrees.
195 Since the angle is "known" to the scanner, it is accounted for and the output values
196 would then correspond to the actual axial velocity that we are seeking. The sample gate
197 size was first set to be that of the vessel's diameter. Once the gate size was set, the
198 time-averaged mean velocity (TAMn), systolic peak velocity, and diastolic velocity were
199 recorded. The resulting Doppler waveform is shown in Fig. 1c.

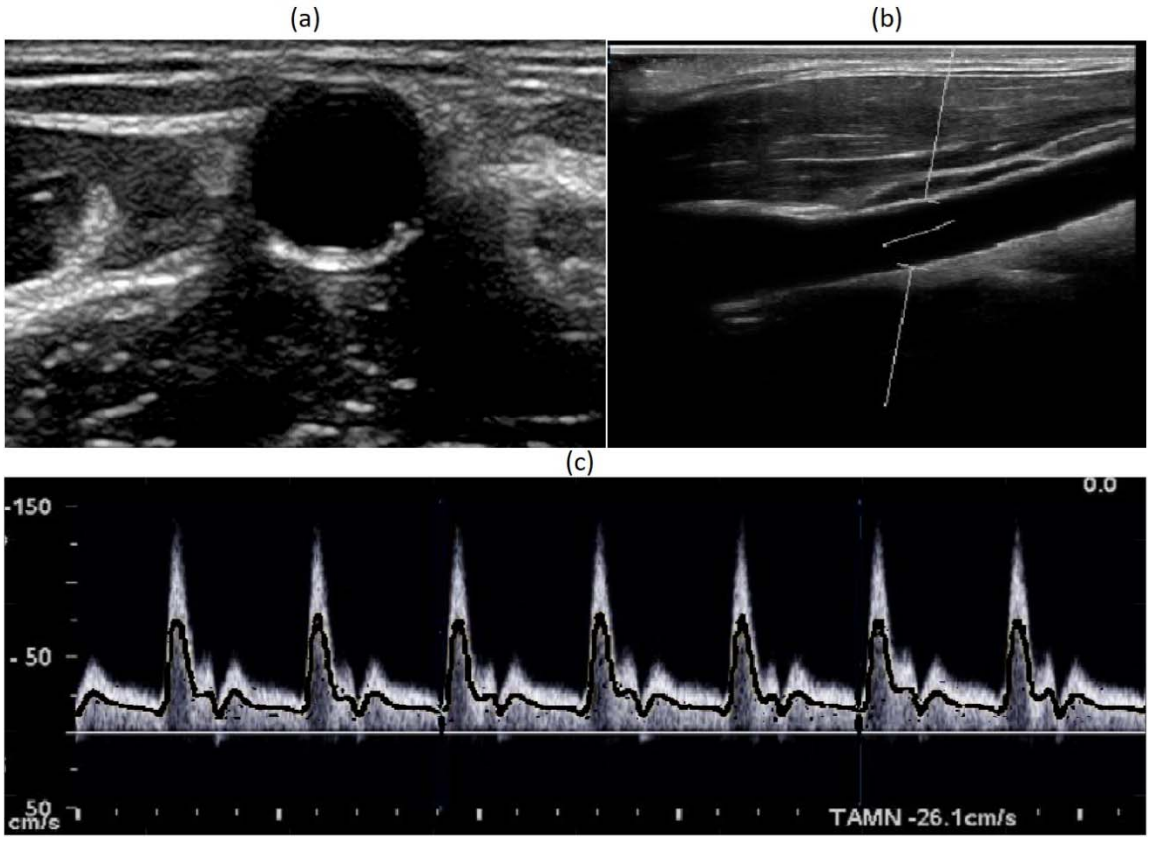

Figure 1: (a), A cross-sectional view of the artery. (b), A longitudinal view of the carotid artery with the measurement window spanning the entire diameter (5.8 mm). The sample line can be seen halfway across from either side of the measurement window. (c), Waveform of the velocity resulting from the measurement shown in (b). x-axis: The interval between two consecutive bold markers represent 1 second. y-axis: Velocity (cm/s).

The output waveform in Fig. 1c consists of consecutive columns of bright and dim pixels, with one column for every instant in time. The brightness of each individual pixel indicates the relative population of red blood cells (RBCs) having a velocity in the neighborhood of that pixel, as indicated by its vertical position in Fig 1c. The average velocity over the entire population of RBCs that occupy the diameter at the instant, corresponding to a column of pixels, is then computed by the scanner, collapsing that

column into a point belonging to the black trace shown in Fig 1c. Mathematically, the black trace in Fig. 1c plots the following function of time:

$$f(t) = \frac{\int_{-R}^{R} \rho_{rbc} v_z(r,t) dr}{\int_{-R}^{R} \rho_{rbc} dr} \quad 1)$$

where R is the vessel radius, ρ_{rbc} is the linear density of the RBCs (RBC/m), and v_z is the axial component of the velocity vector. The monitored vessels in this work were the brachial and carotid arteries whose diameters ranged from 2.8 mm to 6.3 mm. At this scale, it is reasonable to assume that the RBC's are evenly distributed throughout the vessels diameter. In other words, ρ_{rbc} in Eq. (1) is a constant. Hence:

$$f(t) = \frac{\int_{-R}^{R} v_z(r,t) dr}{\int_{-R}^{R} dr} \quad 2)$$

Allowing for axisymmetry, Eq. (2) is reduced to

$$f(t) = \frac{1}{R} \int_{0}^{R} v_z(r,t) dr \quad 3)$$

It is worth noting that $f(t)$ is not the flow-rate-averaged velocity. In other words, multiplying $f(t)$ by the cross-sectional area does not give the flow rate. However, $f(t)$ is the most compact form in which velocity data provided by the scanner could be adapted to the theoretical model.

2.2. Localized Doppler ultrasound imaging

While at the same cross section, the sample gate size was subsequently reduced to the smallest size possible, and the sample line was placed at several chosen radial locations. An example is shown in Fig. 2a. The small size of the window (1mm) makes it

reasonable to assume that the local velocity at that position is the same as the average velocity computed by the scanner.

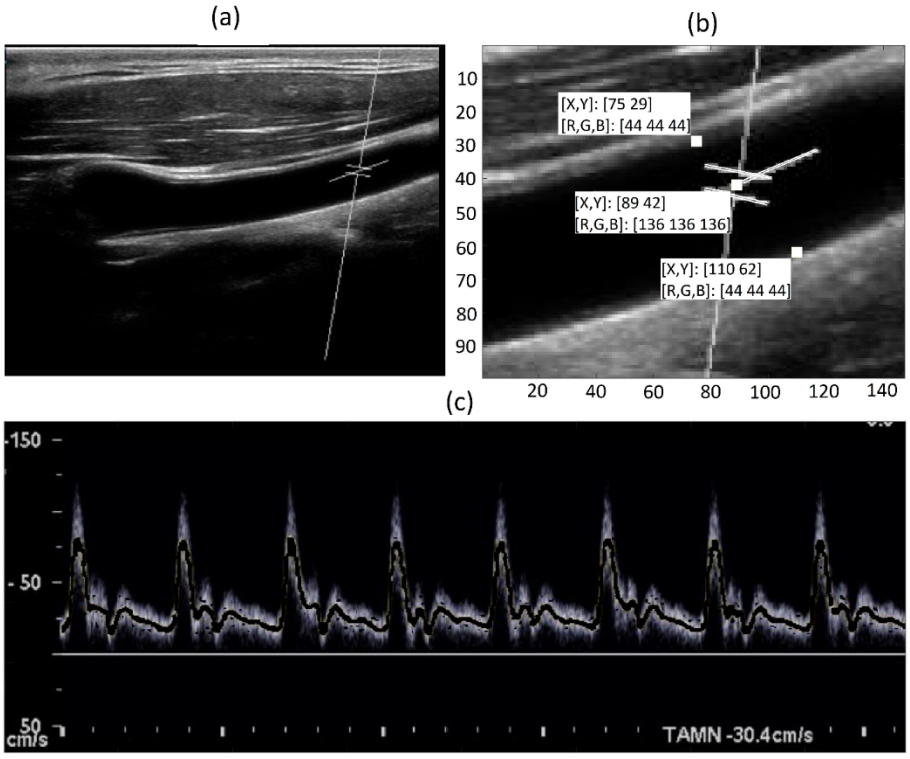

Figure 2: (a), A longitudinal view of the carotid artery (Diameter: 5.8 mm) with the measurement window narrowed down (1 mm) around the location of interest. (b), Using pixel coordinates to compute the radial locations of the measurement window's center. The figure is obtained by reading the ultrasound image in MATLAB©. (c), Waveform of the velocity resulting from the measurement shown in (a).

The radial position, was then computed using the coordinates of three aligned pixels as shown in Fig. 2b. If denotes the distance from the upper pixel to the one in the middle, and denotes the distance from the latter to the bottom pixel, then

(4)

It should be noted that the radius R was measured separately, and it is in fact periodically changing with every cardiac cycle. However, the change in the radius is measured to be within less than 2% from the average value. The vessels were therefore treated as rigid tubes in the theoretical section of this paper. It is also noted that, any set of three pixels that include the one in the middle of the local measurement window can be used to deduce the radial location, as long as they are aligned. This is simply done by using similar triangle ratios to work out the expression in Eq. (4). Since a set of three aligned pixels was not always available in such a way that their line was perpendicular to the vessel, the more general case where they are just required to be aligned was dealt with and hence illustrated in Fig. 2.

Fig 2c. shows the local TAMn measured by the scanner. This local waveform will be used to compare with the analytically predicted velocity profile for the verification of the theoretical model.

3. Formulation

The blood flow is modelled as a pulsatile, laminar, incompressible, Newtonian fluid [38] flowing in a rigid tube of radius, R. The flow was assumed to be periodic and fully developed, i.e. zero radial and orthoradial components of the velocity field. A pulsatile pressure gradient driving the flow, takes the following form

$$\frac{\partial p}{\partial z} = -Ce^{i\omega t} \tag{5}$$

where C is a constant. It is noticed that only the real part of all mentioned quantities is relevant in the equations. For this problem, the resulting axial velocity is given in Ref. [29]:

$$v_z(r,t) = \frac{C}{i\omega\rho}\left[1 - \frac{J_0\left(i^{\frac{3}{2}}\alpha\frac{r}{R}\right)}{J_0\left(i^{\frac{3}{2}}\alpha\right)}\right]e^{i\omega t} \tag{6}$$

where ω is the radial frequency, and α is the Womersley number given by $\alpha = R\sqrt{\frac{\omega\rho}{\mu}}$.

For any random, but periodic pressure gradient of period T, one may decompose it into a Fourier series to fit to the actual pressure gradient. In complex form:

$$-\frac{\partial p}{\partial z}(t) = A_0 + \sum_{n=1}^{N} D_n e^{i\theta_n} e^{i\omega_n t} \tag{7}$$

where $\omega_n = \frac{2\pi n}{T}$.

Making use of the linearity of the problem, and the fact that the A_0 term in Eq. (7) corresponds to the steady component of the pressure gradient, the respective solutions to A_0 and each of the terms inside the summation can be superposed as follows:

$$v_z(r,t) = \frac{A_0 R^2}{4\mu}\left(1 - \frac{r^2}{R^2}\right) + \sum_{n=1}^{N} \frac{C_n}{i\omega_n\rho}\left[1 - \frac{J_0\left(i^{\frac{3}{2}}\alpha_n\frac{r}{R}\right)}{J_0\left(i^{\frac{3}{2}}\alpha_n\right)}\right]e^{i\omega_n t} \tag{9}$$

where:

$$C_n = D_n e^{i\theta_n} \qquad \alpha_n = R\sqrt{\frac{\rho\omega_n}{\mu}} \tag{10}$$

The first term on the right-hand side of Eq. (9) is the parabolic solution to the Poiseuille's flow driven by a constant pressure gradient:

$$\frac{\partial p}{\partial z} = -A_0 \tag{11}$$

The data provided by the scanner was the average velocity over the span of the measurement window as shown in Figs. 1b and 2a. When the window size is set to be that of the vessel's diameter, the black trace in Fig. 1c represents the $f(t)$ in Eq. (3). Before proceeding, all experimental velocity signals were exactly reproduced with the first 60 harmonics ($N = 60$) of their Fourier expansions.

Since the location where the velocity measurement was performed is far enough downstream from the heart, it is reasonable to assume full hydrodynamic development of the flow. Substituting Eq. (9) into Eq. (3) yields

$$f(t) = \frac{A_0 R^2}{6\mu} + \sum_{n=1}^{N} \frac{C_n}{i\omega_n \rho}(1 - F_n)e^{i\omega_n t} \tag{12}$$

where:

$$F_n = \int_0^R \left[\frac{J_0\left(i^{\frac{3}{2}}\alpha_n \frac{r}{R}\right)}{RJ_0\left(i^{\frac{3}{2}}\alpha_n\right)} \right] dr \tag{13}$$

The experimentally obtained $f(t)$ is then broken into a Fourier series:

$$f(t) = A_{f0} + \sum_{n=1}^{N} D_{fn} e^{i\theta_{fn}} e^{i\omega_n t} \tag{14}$$

Finally, by matching Eq. (12) with Eq. (14), the unknown A_0 and C_n can be obtained:

$$A_0 = \frac{6\mu A_{f0}}{R^2} \qquad C_n = \frac{i\omega_n \rho D_{fn} e^{i\theta_{fn}}}{1 - F_n} \tag{15}$$

Eq. (15) is then substituted into Eq. (9) to obtain the theoretical prediction of the velocity field.

Different from our method outlined in Eqs. (12-15), Refs. [35-37] used the measured centerline velocity to back-calculate the velocity field. Substituting $r = 0$ in Eq. (9) yields the theoretical centerline velocity $V_c(t)$ as:

$$V_c(t) = \frac{A_0 R^2}{4\mu} + \sum_{n=1}^{N} \frac{C_n}{i\omega_n \rho} \left[1 - \frac{1}{J_0\left(i^{\frac{3}{2}}\alpha_n\right)} \right] e^{i\omega_n t} \tag{16}$$

The measured centerline velocity $V_{exp}(t)$ is again, broken into a Fourier series:

$$V_{exp}(t) = A_{c0} + \sum_{n=1}^{N} D_{cn} e^{i\theta_{cn}} e^{i\omega_n t} \tag{17}$$

Similarly, by matching Eq. (16) with Eq. (17) A_0 and C_n can be obtained:

$$A_0 = \frac{4\mu A_{c0}}{R^2} \qquad C_n = \frac{i\omega_n \rho D_{cn} e^{i\theta_{cn}}}{1 - \frac{1}{J_0\left(i^{\frac{3}{2}}\alpha_n\right)}} \tag{18}$$

The problem with this method is that it only accounts for the flow behavior at a very narrow central region in the blood vessel. As evidenced by the comparison performed later, the DA velocity as an input to Womersley's model, leads to a better agreement between predicted and measured local velocities.

4. Results and discussion

The black trace $f(t)$ in Fig. 1c was broken into a Fourier series according to Eq. (14). Then, the coefficients A_0 and C_n were computed using Eq. (18), which were further substituted into Eq. (9) to obtain the analytical predictions of the velocity profile. The radial positions, at which the local measurements were made, were obtained based on the pixel coordinates as shown in Fig. 2b and calculated using Eq. (4). Each of the

calculated radial positions, r, were then substituted into Eq. (9) to obtain the theoretical prediction of the local velocity, which was later compared to the experimental data shown as the black trace of Fig. 2c. A similar procedure is followed to obtain the analytical velocity profiles from the measured centerline velocity which was broken into a Fourier series (Eq. (17)). A_0 and C_n which are obtained from Eq. (18), were substituted in Eq. (9) to get the analytical velocity profile.

Fig. 3 shows the velocity behavior at a specific radial location of the brachial artery, $\frac{r}{R} = 0.047$, throughout a complete cardiac cycle. Different possible values of human blood viscosity were considered, μ= 1 cP, 2.5 cP and 4 cP for computation. It shows that the analytical predictions with different values of blood viscosity are very close to each other, and the analytical model agrees well with the experimental data. The observed low sensitivity of the local velocity to the blood viscosity is attributed to the fact that, the measured mean velocity has the highest impact on the velocity distribution; with the same mean velocity, the velocity profile is defined. The good agreement between the analytical model and the experimental data demonstrates the validity of the theory. The slight difference between the analytical model and the experimental measurements is attributed to the fact that cardiac cycles are not perfectly rhythmic. In the current study, we assume the blood to be a Newtonian fluid. This assumption is supported by extensive literatures. For example, the Newtonian model of blood was numerically compared with four non-Newtonian models for a pulsatile flow in the presence of arterial stenosis [38]. The results showed that the deviation of all four non-Newtonian models from the Newtonian behavior was negligible for the case of pulsatile flow and thus provide justification for the Newtonian assumption.

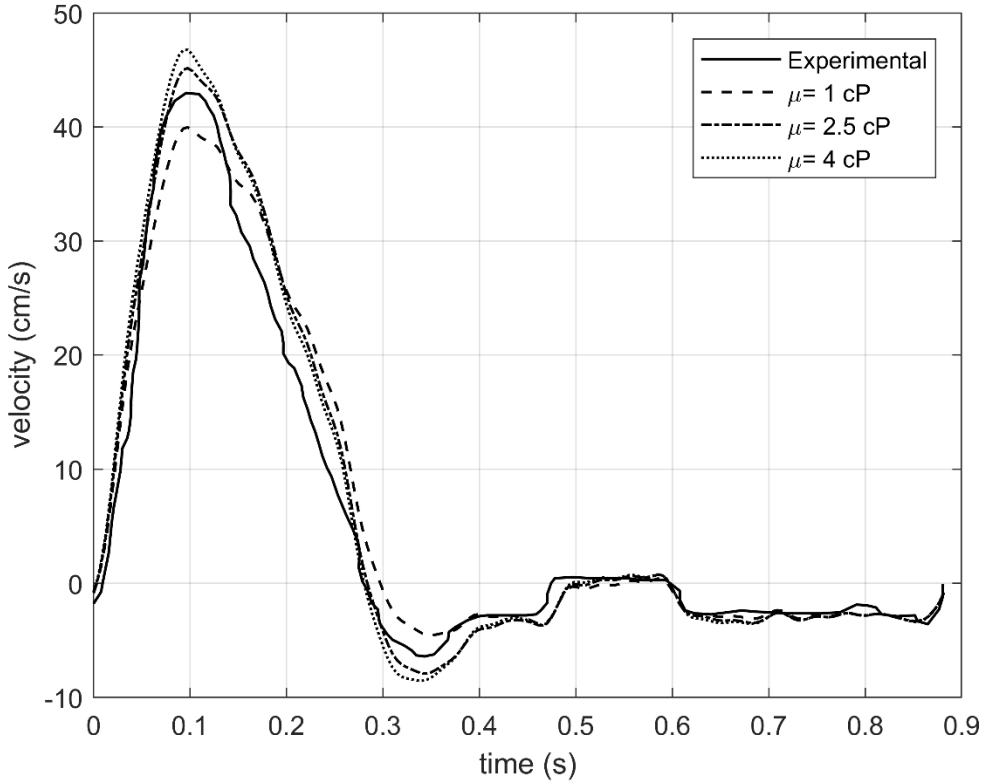

Figure 3: Comparison of the analytical solution for different values of viscosity, with experimental data for the time dependent velocity in the brachial artery at r/R=0.047 where R=1.4 mm

Fig. 4 shows representative results for the comparison between the analytical velocity profile and the experimental data at three radial locations, $\frac{r}{R} = 0.047$, 0.64, and 0.69, respectively, in the brachial artery at the peak systole of the cardiac cycle. The blood viscosity, μ= 1 cP. The variation of the experimental data at the same location confirms that, cardiac cycles are not completely identical. The analytical model shows that the blood velocity reaches its maximum at the center of the blood vessel, r=0, and gradually decreases with the increase of distance away from the center. The rate of change in the velocity increases sharply near the vessel wall and becomes zero when r= R. Fig. 4 shows that the analytical prediction agrees very well with the experimental

335 data. The observed slight difference between them might arise from the non-
336 synchronized measurement of average and local velocities, as shown in Figs 1 and 2,
337 respectively.

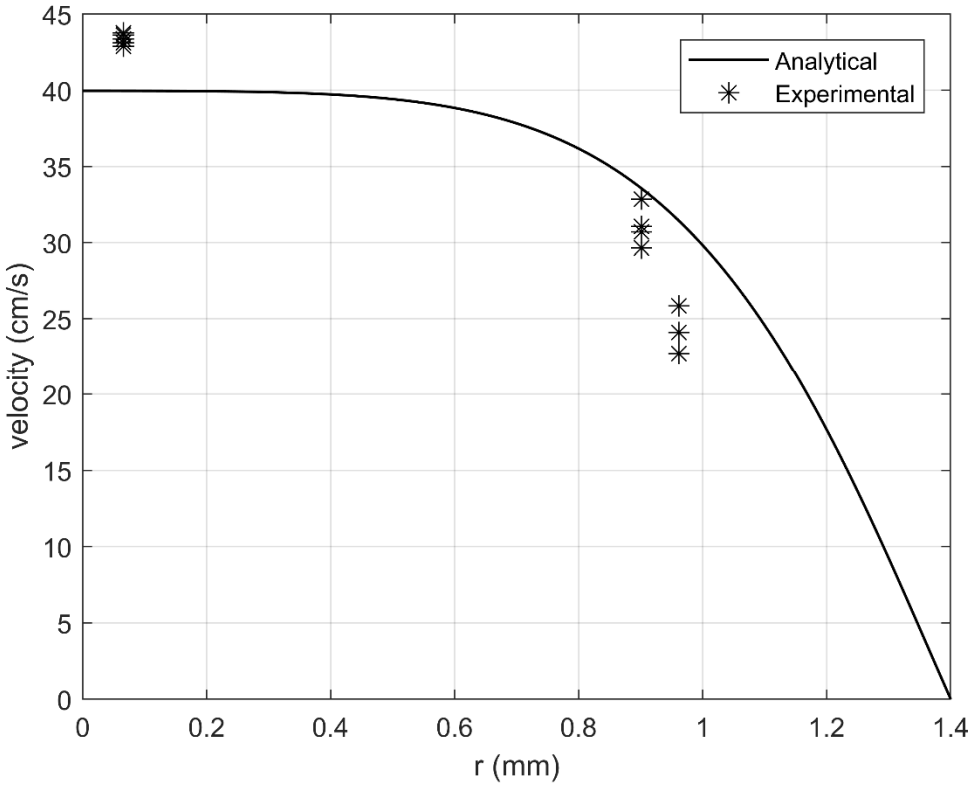

338

339 **Figure 4:** Comparison of the analytical solution with experimental data at the peak
340 systole of the cardiac cycle for 3 radial locations in the brachial artery: r/R = 0.047, 0.64,
341 and 0.69 where R=1.4 mm

342 To further examine the accuracy of the model, a scatter plot of the analytical vs.
343 experimental velocities corresponding to the data of Fig. 3, is shown in Fig. 5. Since the
344 effect of viscosity on the predicted time-dependent velocity was shown to be minimal,
345 the analytical curve corresponding to a viscosity of 1 cP in Fig. 3, was chosen for the
346 comparison in Fig. 5. The slope of 0.98 of the regression line, as well as its small

intercept value, 1.68 cm/s (4.2% of maximum measured velocity), show a reliable prediction of the experimental velocities with a very slight bias. The tightness of the scatter around the regression line is indicated by a high R-squared value of 0.96.

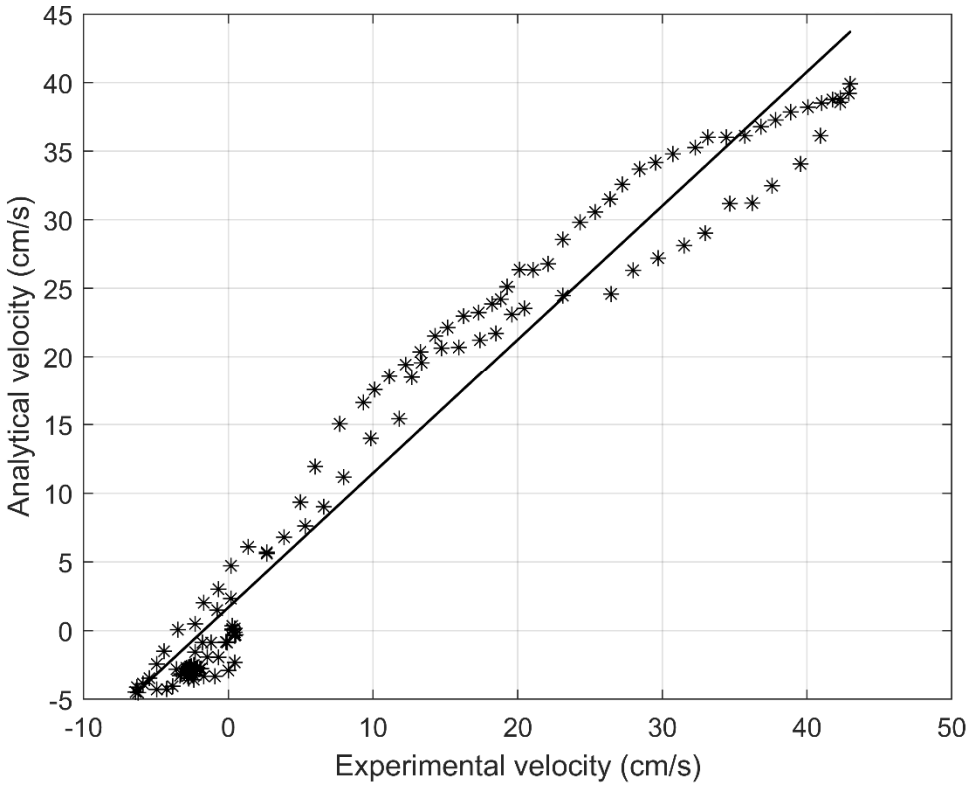

Figure 5: A scatter plot showing a statistical version of the comparison in Fig. 3 with an added regression line: slope = 0.98, intercept = 1.68 cm/s (4.2% of the maximum measured velocity), R-squared = 0.96

To demonstrate the better suitability of the DA velocity as a more appropriate input to Womersley's [29] equations, the same procedure described above to obtain the instantaneous local velocity predictions from the acquired DA velocity (Eqs. (12-15)), was applied to the centerline velocity (VC) (Eqs. (16-18)). Figs. 6a and 6b show a sample comparison (The solid straight line is the first bisector (y = x)) of the two

approaches in the brachial artery referred to in Figs. 3-5, where the difference in the error is clearly illustrated by the scatter plots. The DA approach led to an RMS error of 9.87 % (Fig 6a), whereas the error corresponding to the VC approach was 17.4% (Fig 6b). Fig. 6c shows the wall shear rate, resulting from both methods over one cardiac cycle. An almost 50% difference in the systolic (typically of the most clinical relevance) wall shear rate is observed. In view of the better agreement with experimental data, shown in Fig. 6a, the systolic WSS resulting from the DA method would therefore be considered closer to the actual value, and thus more reliable.

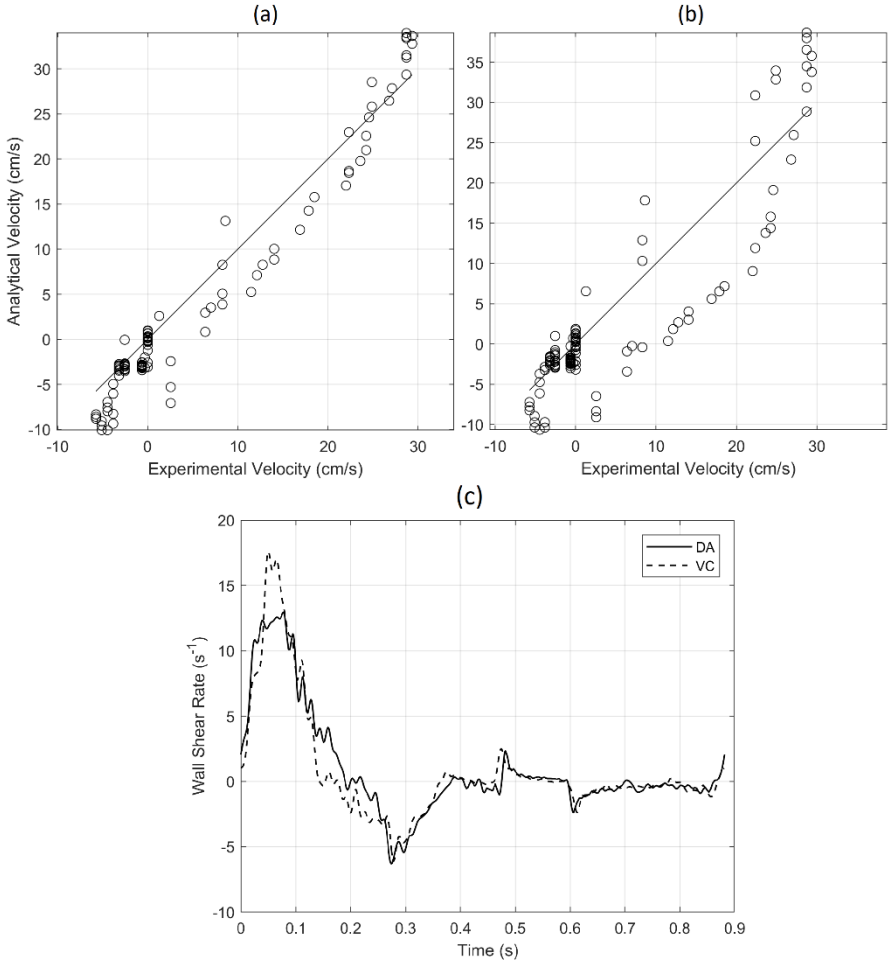

Figure 6: Predicted local velocity versus the one measured experimentally, in the brachial artery at r/R = 0.64 where R = 1.4mm.

(a): using the DA velocity, RMS error = 9.87%, (b): using VC, RMS error = 17.4%
(c): Wall shear rate where the systolic difference between the two methods is 49.8%

The Root Mean Square (RMS) errors and R-squared values for both approaches are compared in Table 1. In most of the cases, the proposed DA approach outperformed the traditional VC approach, in regard to both criteria of RMS errors and R-squared values. Out of the three cases (Br-1, Ca-3, and Ca-6) where the error corresponding to the current DA approach exceeded that of the VC approach, only one (Ca-6) was substantial. For all the cases shown in Table 1, the R-squared values corresponding to the DA approach either exceeded or tied with (in the Br-1 case) the VC approach. This is interpreted as the DA velocity approach having a better predictability for the deviation from experimental results, even when the error is higher than that of the VC approach. An important point needs to be made at this stage. The uncertainties involved in this study apply to both approaches, which validates the conclusion that the presented approach yield a better performance in predicting the velocity profile.

Table I. RMS errors and R-Squared values with their corresponding differences, resulting from the presented DA velocity approach, and the VC approach.

	RMS error (%)		*Difference from VC (%)*	*R-Squared*		*Difference from VC (%)*
	DA	**VC**		**DA**	**VC**	
Br-1	12.86	11.15	15.34	0.95	0.95	0.00
Br-2	17.09	24.3	-29.67	0.96	0.8	20.00
Br-3	9.87	17.4	-43.28	0.95	0.82	15.85
Br-4	13.8	20.41	-32.39	0.94	0.81	16.05
Ca-1	29.64	49.6	-40.24	0.6	0.32	87.50
Ca-2	24.73	28.74	-13.95	0.74	0.51	45.10
Ca-3	28.72	25.09	14.47	0.76	0.53	43.40
Ca-4	23.31	40.77	-42.83	0.95	0.86	10.47
Ca-5	17.41	16.16	7.74	0.93	0.77	20.78

Ca-6	33.98	22.86	48.64	0.96	0.92	4.35

387

388 In Fig. 7, the wall shear stress, based on the DA approach applied to the brachial
389 artery of Fig. 3, is plotted versus time throughout a cardiac cycle. The WSS, τ_w profiles
390 were calculated based on the constitutive equation of the blood, $\tau_w = \mu(\partial v_z/\partial r)_{r=R}$ at
391 two representative viscosity values, μ = 2.5 cP and 4 cP. The time-averaged absolute
392 WSS corresponding to a viscosity of 2.5 cP, is about 8.51 dyn/cm2; while that
393 corresponding to 4 cP is about 13.62 dyn/cm2. It is important to note that the peak
394 systolic WSS determined by our approach in Fig. 7 is consistent with previously
395 reported vascular systolic WSS values of 5.03 N/m2 (50.3 dyn/cm2) for men, and 5.31
396 N/m2 (53.1 dyn/cm) for women [39].

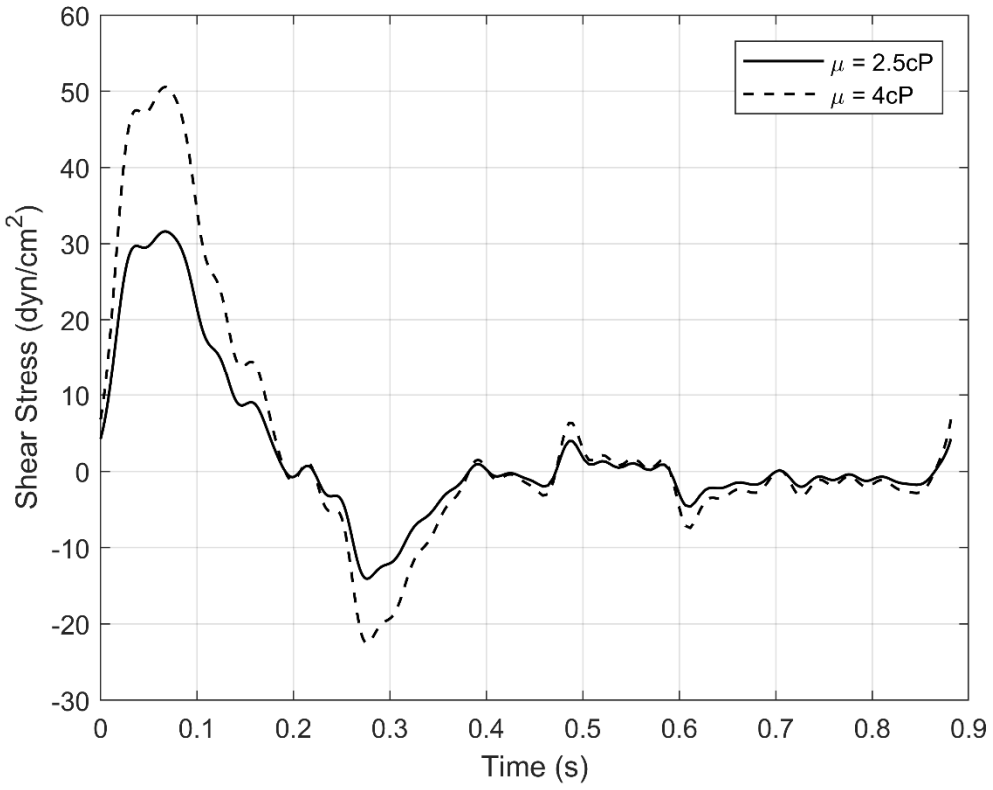

397

Figure 7: The WSS in the brachial artery referred to in Fig. 3, throughout a cardiac cycle, for two limiting values of the normal range of human blood viscosity

Altogether, forty local measurements were performed that cover both brachial and carotid arteries on four healthy subjects. Consistent results similar to the ones presented in Figs. 3, 4 and 5 were obtained. In the appendix, we have included representative results for carotid arteries. It is instructive to present a complete and comprehensive scatter plot which includes the data of Fig. 5 as part of a larger sample covering all the subjects and totaling 3278 data points. The result is shown in Fig. 8. It is clearly shown in this figure that, the data are centered on the regression line with a slope of about 0.97, and a relatively very small intercept value of about 1.71 cm/s which is 1.89 % of maximum measured velocity thereby providing strong evidence in support of the proposed approach.

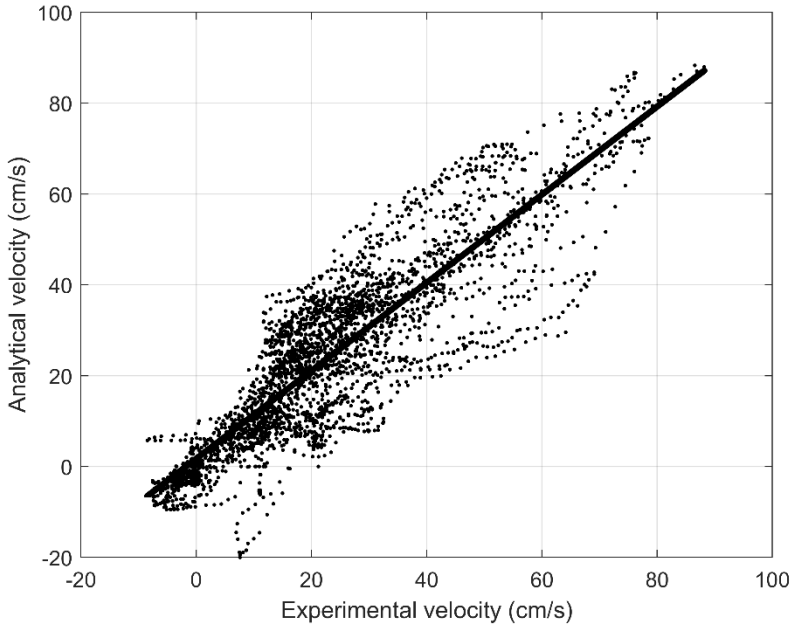

Figure 8: A scatter plot showing a more comprehensive version of the comparison in Fig. 5 with an added regression line: slope = 0.97, intercept = 1.71 cm/s (1.89 % of maximum measured velocity), R-squared = 0.79

It is worth noting that, the main purpose behind seeking an accurate prediction of the velocity profile is the subsequent accurate prediction of local WSS, based on the constitutive equation of the blood. Hence, the most important outcome of this paper can be inferred from Fig. 8, where data points that cover all 4 subjects and all considered distances from the vessel wall, are especially tight at very low velocities. In view of the fact that the regions near the wall are low velocity regions, the high robustness of the presented technical approach in predicting the flow field near the wall and consequently the WSS, becomes noticeable statistically.

The limitations of this study primarily arise from sources of uncertainty in the measurements. The most significant one is the unsynchronized measurements of both average and local velocities. Because the cardiac cycles are not completely identical, matching the local velocity measured at one time with the one theoretically predicted based on the average velocity measured at a different time, will inevitably introduce errors. Another source of error arises from the local velocity measurements near the vessel wall. Due to the slight periodic change of the diameter some of the surrounding tissue is inevitably included in that window used to measure a local velocity. Other factors that influence the results are non-perfect circular cross-section of the vessels (Fig. 1a), as well as the viscosity fluctuations during cardiac cycles since blood is a shear thinning fluid. It should be emphasized that the presented method applies only to relatively straight sections of blood vessels with minimal curvature, where Womersley's solution can be reasonably assumed to capture the flow field. Evidently, there are cases

in which the vessel where the WSS needs to be estimated cannot be reliably scanned using this technique. Coronaries for instance, which are continuously moving with the heart's muscle make it impossible to take a steady image even if both the amplitude and frequency of the ultrasound waves are set to reach that depth. Despite of these limitations, the non-invasive, experimental and analytical approach presented herein provides an accurate and reliable prediction of the blood velocity field, which would then be useful for predicting the WSS if the blood viscosity is measured separately. WSS has been demonstrated to be a potential marker to identify various cardiovascular diseases. The paper presented herein, precisely capturing the fundamental flow physics in arteries, could be readily translated to clinical applications where Doppler ultrasound imaging is used to estimate WSS.

5. Conclusion

To recap, in this study, the carotid and brachial arteries of healthy subjects were monitored using the technique of Doppler ultrasound imaging. The diameter of the arteries ranged from 2.8 mm to 6.3 mm. The average velocity over the entire diameter was acquired experimentally, to which the classical Womersley's solution for a pulsatile flow in a rigid pipe was adapted to obtain the theoretical prediction of the velocity profile. Localized Doppler ultrasound imaging was used to obtain the detailed velocity measurements at various radial locations. Very good agreement was observed between the experimental results and the theoretical predictions, especially evidenced by the scatter plot where one finds that, most of the data points are tightly close to the regression line of a slope of 0.97, with a slight bias indicated by the relatively small intercept value of 1.71 cm/s. The same procedure was then repeated with the centerline

458 velocity being the input to Womersley's equations. It was found that using the DA
459 velocity, rather than the center-line velocity, yields a better prediction for the velocity
460 field, and consequently the WSS.

461 The novelty and features of this paper are outlined as follows:

462 • The experimental validation of theoretical velocity predictions was made in near-
463 real-time, where *in vivo* local velocity measurements were compared to the
464 analytical local velocities.
465 • The DA velocity was used as an input to the theoretical model to obtain the
466 instantaneous pressure gradient, rather than using the centerline velocity that
467 inevitably brings noise/errors in measurements.
468 • The TAMn trace was more appropriately interpreted as the DA velocity, rather
469 than the flow averaged velocity that would give the flow rate when multiplied by
470 the vessel's cross-sectional area; which explains the better performance of the
471 presented approach.

472 The main contributions of this paper are summarized as follows:

473 • The combined analytical and experimental approach provides a novel, much
474 more reliable, cheap, and non-invasive method to precisely capture the
475 instantaneous velocity profile in large blood vessels, hence allowing for a more
476 accurate estimation of WSS.
477 • The *in vivo* near-real-time local velocity measurements provides a much more
478 realistic description of the blood velocity, as compared to the ones using flow
479 phantoms.

480

481 ## Acknowledgements

482 The authors would like thank Dr. Chengyu Li for his constructive comments about
483 image based CFD. B.S. is partially supported by the sponsorship of the James R. Birle
484 Chair in Energy Technology. This research was supported by the National Science
485 Foundation under Award No.1511096.

486

487

488

489

490

491

492

493

494

495

496

497

498

499

500

501

502

APPENDIX

To illustrate the generality of the cases presented in the main text, an additional set of data is shown in this appendix.

In Fig. A.1, local velocity predictions were compared to local measurements at the peak systole for 6 radial locations in the carotid artery of the subject aged 27. The analytical profile compares very well with the experimental data and following the same trend.

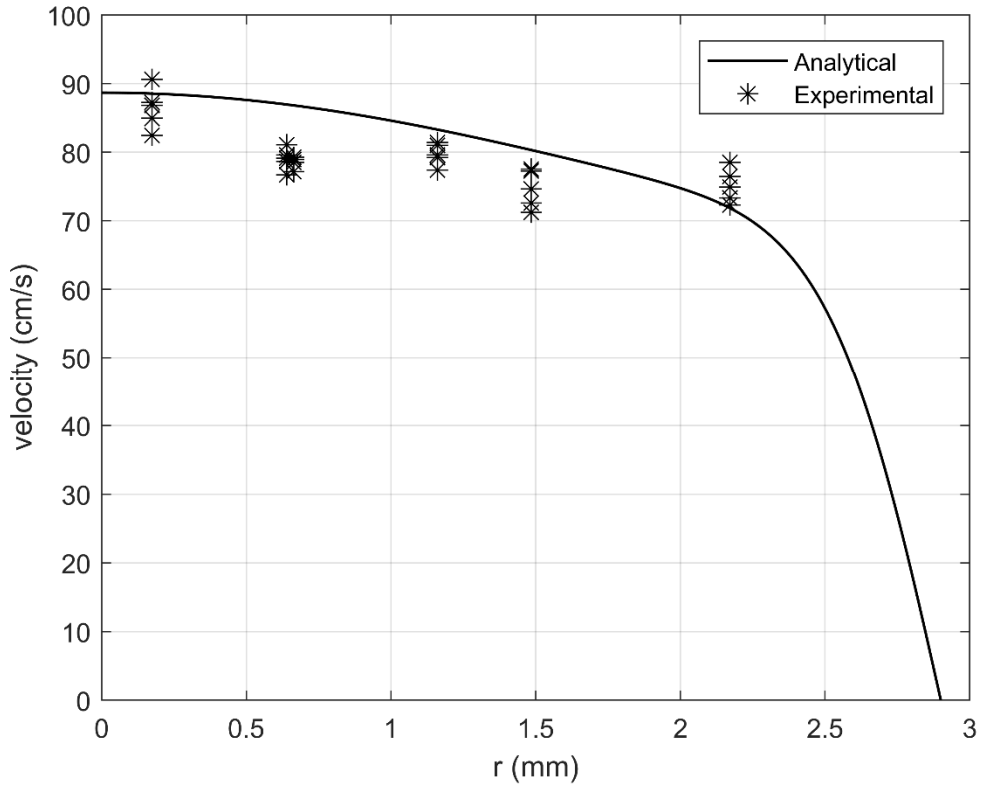

Figure A.1: Comparison of the analytical solution with experimental data at the peak systole of the cardiac cycle for 6 radial locations in the carotid artery: r/R = 0.06, 0.22, 0.23, 0.4 0.51, and 0.75 where R=2.9 mm

Temporal predictions for the carotid artery are compared with measurements in Fig A.2, almost half-way between the central axis and the wall. Except around t = 0.2s, the temporal velocity prediction agrees very well with experimental measurements.

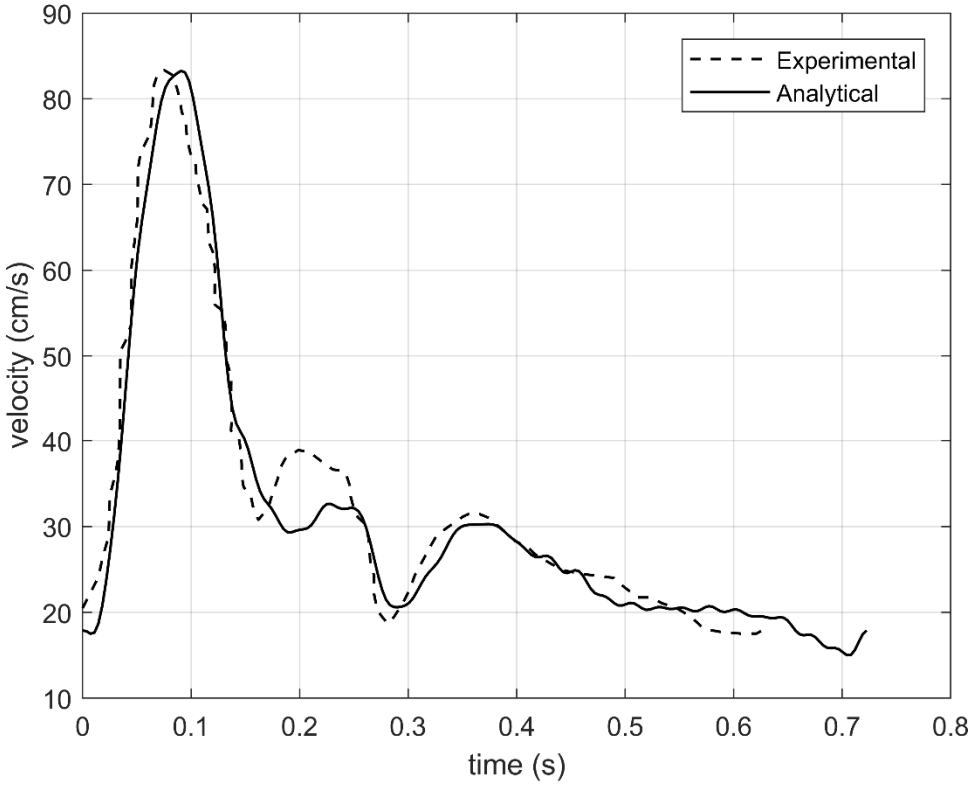

Figure A.2: Comparison of the analytical solution with experimental data for the time dependent velocity in the carotid artery at r/R=0.4 where R=2.9 mm

The comparison in Fig. A.2 is laid on a scatter plot as shown in Fig. A.3. Similarly, to the data in Fig. 6, the regression line has a slope that is close to 1 with a very small bias indicated by the intercept value. The data points are fairly tight around the regression line which is suggested by an R-squared value of about 0.92.

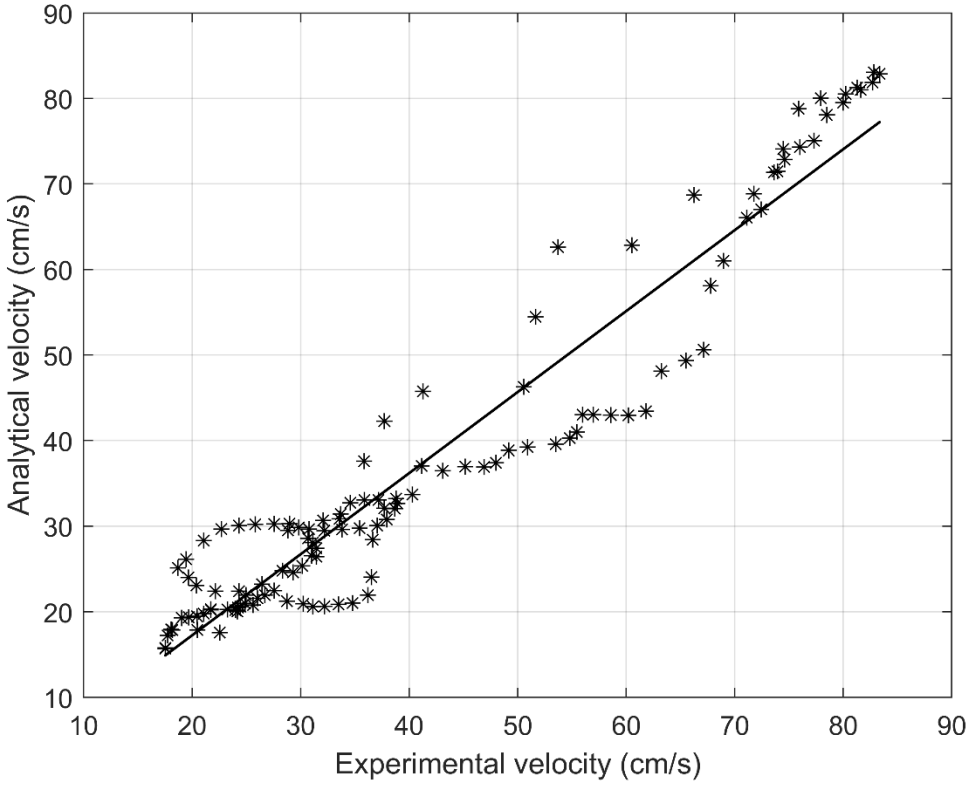

526

527 **Figure A.3:** A scatter plot showing a statistical version of the comparison in Fig. A2 with
528 an added regression line: slope = 0.95, intercept = -1.69 cm/s (2.01 % of the maximum
529 measured velocity), R-squared = 0.92

530 In Fig. A.4, the wall shear stress based on the predicted instantaneous velocity
531 profile corresponding to the carotid artery of Fig. A.2, is plotted versus time throughout a
532 cardiac cycle. The time-averaged absolute WSS corresponding to a viscosity of 2.5 cP,
533 is about 17.78 dyn/cm^2; while that corresponding to 4 cP is about 28.45 dyn/cm^2

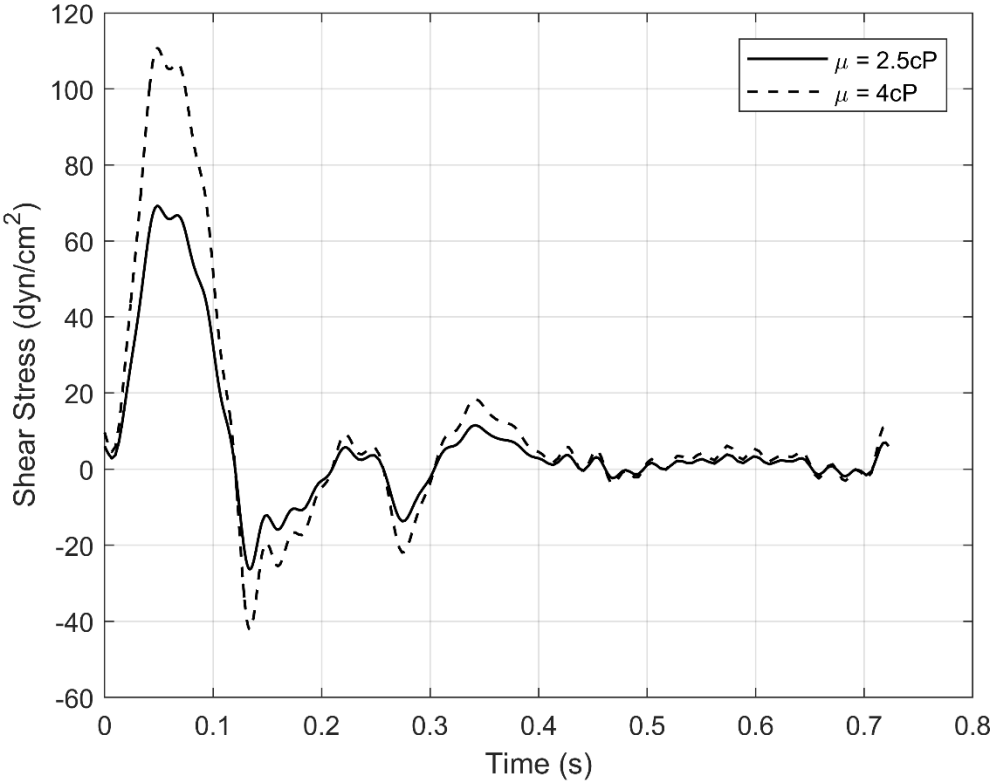

534

535 **Figure A.4:** The WSS in the carotid artery referred to in Fig. A2, throughout a cardiac
536 cycle, for two limiting values of the normal range of human blood viscosity

537 For each local measurement (r/R), systolic velocity data were collected and
538 averaged. The standard deviation (SD) for each, is presented as a percentage from that
539 corresponding average. The results are shown below:

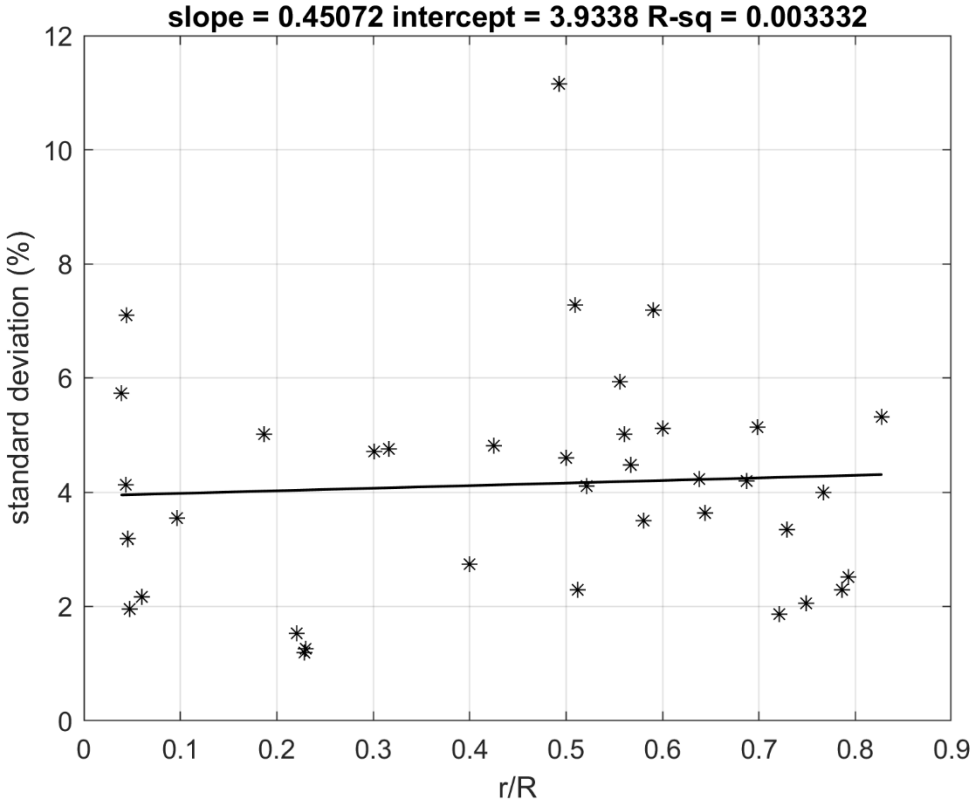

Figure A.5: Standard deviation from the average measured systolic velocities as a function of dimensionless radial position

The mean SD is about 4.13 %. The slope of the regression line shows a flat to very small sensitivity to the dimensionless radial location increasing by 0.45% from centerline to wall.

Modeling the spread distribution in SD to be Gaussian this would result in a 95% confidence interval for the standard deviation to be, between 0.24% and 8.01%.

Applying the same interval to the entire cardiac cycle would then result in that same interval of uncertainty, for the wall shear stress.

552 # References

[1] Chien, S. Mechanotransduction and endothelial cell homeostasis: The wisdom of the cell. Am J Physiol-Heart C 2007;292(3):H1209-24.

[2] Tarbell JM, Weinbaum S, Kamm RD. Cellular Fluid Mechanics and Mechanotransduction. Ann Biomed Eng 2005;33(12):1719-23.

[3] Weinbaum S, Zhang X, Han Y, Vink H, Cowin SC. Mechanotransduction and flow across the endothelial glycocalyx. P Natl Acad Sci 2003;100(13):7988-95.

[4] Shi Z, Abraham G, Tarbell JM. Shear stress modulation of smooth muscle cell marker genes in 2-d and 3-d depends on mechanotransduction by heparan sulfate proteoglycans and erk1/2. PLoS ONE 2010;5(8):e12196.

[5] Davies, PF. Hemodynamic shear stress and the endothelium in cardiovascular pathophysiology. Nat Clin Pract Card 2008;6(1):16-26.

[6] Gnasso A, Irace C, Carallo C, Franceschi MS, Motti C, Mattioli PL, Pujia A. In vivo association between low wall shear stress and plaque in subjects with asymmetrical carotid atherosclerosis. Stroke 1997;28(5):993-98.

[7] Odonnell TF. Pulsatile flow and atherosclerosis in the human carotid bifurcation: Positive correlation between plaque location and low and oscillating shear stress. J Vasc Surg 1986;3(6):944.

[8] Wentzel JJ, Whelan DM, Giessen WJ, Beusekom HM, Andhyiswara I, Serruys PW, Slager CJ, Krams R. Coronary stent implantation changes 3-D vessel geometry and 3-D shear stress distribution. J Biomech 2000;33(10):1287-95.

[9] Wentzel JJ, Krams R, Schuurbiers JC, Oomen JA, Kloet J, Giessen WJ, Serruys PW, Slager CJ. Relationship between neointimal thickness and shear stress after wallstent implantation in human coronary arteries. Circulation 2001;103(13):1740-45.

[10] Ooij PV, Potters WV, Nederveen AJ, Allen BD, Collins J, Carr J, Malaisrie SC, Markl M, Barker AJ. A methodology to detect abnormal relative wall shear stress on the full surface of the thoracic aorta using four-dimensional flow MRI. Magn Reson Med 2014;73(3):1216-27.

[11] Carter HH, Atkinson CL, Heinonen IH, Haynes A, Robey E, Smith KJ, Ainslie PN, Hoiland RL, Green DJ. Evidence for shear stress–mediated dilation of the internal carotid artery in humans. Hypertension 2016;68(5):1217-24.

[12] Farag ES, Ooij PV, Planken RN, Dukker KC, Heer FD, Bouma BJ, Robbers-Visser D, Groenink M, Nederveen AJ, de Mol BAJM, Kluin J, Boekholdt SM.

Aortic valve stenosis and aortic diameters determine the extent of increased wall shear stress in bicuspid aortic valve disease. J Magn Reson Imaging 2018; doi:10.1002/jmri.25956

[13] Knobelsdorff-Brenkenhoff FV, Karunaharamoorthy A, Trauzeddel RF, Barker AJ, Blaszczyk E, Markl M, Schulz-Menger J. Aortic flow and wall shear stress in aortic stenosis is associated with left ventricular remodeling. J Cardiov Magn Reson 2016;18 (Suppl 1): Q57.

[14] Cibis M, Potters WV, Selwaness M, Gijsen FJ, Franco OH, Lorza AM, de Bruijne M, Hofman A, van der lugt A, Nedeveen AJ, Wentzel JJ. Relation between wall shear stress and carotid artery wall thickening MRI versus CFD. J Biomech 2016;49(5):735-41.

[15] Timmins LH, Molony DS, Shtehardi PE, Mcdaniel MC, Oshinski JN, Samady H, Giddens DP. Focal association between wall shear stress and clinical coronary artery disease progression. Ann Biomed Eng 2014;43(1):94-106.

[16] Alaraj A, Shakur SF, Amin-Hanjani S, Mostafa H, Khan S, Aletich VA, Charbel FT. Changes in wall shear stress of cerebral arteriovenous malformation feeder arteries after embolization and surgery. Stroke 2015;46(5):1216-20.

[17] Liu Z, Zhao Y, Wang X, Zhang H, Cui Y, Diao Y, Xiu J, Sun X, Jiang G. Low carotid artery wall shear stress is independently associated with brain white-matter hyperintensities and cognitive impairment in older patients. Atherosclerosis 2016;247:78-86.

[18] Restaino RM, Walsh LK, Morishima T, Vranish JR, Martinez-Lemus LA, Fadel PJ, Padilla J. Endothelial dysfunction following prolonged sitting is mediated by a reduction in shear stress. Am J Physiol-Heart C 2016;310(5):H648-53.

[19] Carter HH, Spence AL, Ainslie PN, Pugh CJ, Naylor LH, Green DJ. Differential impact of water immersion on arterial blood flow and shear stress in the carotid and brachial arteries of humans. Physiol Rep 2017;5(10):e13285.

[20] Gizzi A, Bernaschi M, Bini D, Cherubini C, Filippi S, Melchionna S, Succi S. Three-band decomposition analysis of wall shear stress in pulsatile flows. Phys Rev E Stat Soft Matter Phys 2011;83(3 Pt 1):031902

[21] Cibis M, Potters WV, Gijsen FJH, Marquering H, vanBavel E, van der Steen AFW, Nederveen AJ, Wentzel JJ. Wall shear stress calculations based on 3D cine phase contrast MRI and computational fluid dynamics: a comparison study in healthy carotid arteries. NMR Biomed 2014; 27: 826–834.

[22] Barber DC, Hose DR. Automatic segmentation of medical images using image registration: diagnostic and simulation applications. J Med Eng Technol

2005;29(2):53–63.

[23] Brown AG, Shi Y, Arndt A, Muller J, Lawford P, Hose DR. Importance of realistic LVAD profiles for assisted aortic simulations: evaluation of optimal outflow anastomosis locations. Comput Methods Biomech Biomed Engin 2012;15(6):669–80.

[24] Zhao F, Xie X. An Overview on Interactive Medical Image Segmentation. Ann BMVA 2013;7:1–22.

[25] Hecher K, Campbell S, Doyle P, Harrington K, Nicolaides K. Assessment of fetal compromise by doppler ultrasound investigation of the fetal circulation: arterial, intracardiac, and venous blood flow velocity studies. Circulation 1995;91(1):129-138.

[26] Wong KS, Li H, Chan YL, Ahuja A, Lam WW, Wong A, Kay R. Use of transcranial doppler ultrasound to predict outcome in patients with intracranial large-artery occlusive disease. Stroke 2000;31(11):2641-47.

[27] Pederson MM, Phil MJ, Haugaard P, Hansen KL, Lange T, Lonn L, Nielsen MB, Jensen JA. Novel flow quantification of the carotid bulb and the common carotid artery with vector flow ultrasound. Ultrasound Med Biol 2014;40(11):2700-6.

[28] Hudson JM, Williams R, Milot L, Wei Q, Jago J, Burns PN. In vivo validation of volume flow measurements of pulsatile flow using a clinical ultrasound system and matrix array transducer. Ultrasound Med Biol 2017;43(3):579-85.

[29] Womersley JR. Method for the calculation of velocity, rate of flow and viscous drag in arteries when the pressure gradient is known. J Physiol 1955;127(3):553-63.

[30] Mynard JP, Steinman DA. Effect of velocity profile skewing on blood velocity and volume flow waveforms derived from maximum Doppler spectral velocity. Ultrasound Med Biol 2013;39(5):870-81.

[31] Mynard JP, Wasserman BA, Steinman DA. Errors in the estimation of wall shear stress by maximum Doppler velocity. Atherosclerosis 2013;227(2):259-66.

[32] Ponzini R, Vergara C, Rizzo G, Veneziani A, Redaelli A, Vanzulli A, Parodi O. Computational Fluid Dynamics-Based Estimation of Blood Flow Rate in Doppler Analysis: In Vivo Validation by Means of Phase Contrast Magnetic Resonance Imaging. ASME 2009 Summer Bioengineering Conference, Parts A and B. doi:10.1115/sbc2009-205522

[33] Swillens A, Shcherbakova D, Trachet B, Segers P. Pitfalls of doppler measurements for arterial blood flow quantification in small animal research: a

study based on virtual ultrasound imaging. Ultrasound Med Biol 2016;42(6):1399-411.

[34] Ricci S, Swillens A, Ramalli A, Cinthio M, Segers P, Tortoli P. Improved Wall Shear Rate method for robust measurements. 2014 IEEE International Ultrasonics Symposium. doi:10.1109/ultsym.2014.0107

[35] Blake JR, Meagher S, Fraser KH, Easson WJ, Hoskins PR. A method to estimate wall shear rate with a clinical ultrasound scanner. Ultrasound Med Biol 2008;34(5):760-74.

[36] Zhou X, Xia C, Khan F, Corner G, Huang Z, Hoskins PR. Investigation of ultrasound measured flow rate and wall shear rate in wrist arteries using flow phantoms. Ultrasound Med Biol 2016;42(3):815-23.

[37] Yang X, Hollis L, Adams F, Khan F, Hoskins PR. A fast method to estimate the wall shear stress waveform in arteries. Ultrasound 2013;43(3):23-28.

[38] Rabby, M. G., S. P. Shupti, M. M. Molla. Pulsatile non-Newtonian laminar blood flows through arterial double stenoses. Journal of Fluids 2014:1-13.

[39] Silber HA, Bluemke DA, Ouyang P, Du YP, Post WS, Lima JA. The relationship between vascular wall shear stress and flow-mediated dilation: Endothelial function assessed by phase-contrast magnetic resonance angiography. J Am Coll Cardiol 2001;38(7):1859-65.

553